J. Plasma Phys. (2022), *vol*. 88, 175880502
Published by Cambridge University Press

doi:10.1017/S0022377822000836

LETTER

A measurement of the effective mean free path of solar wind protons

Jesse T. Coburn [1],†, **Christopher H.K. Chen** [1] **and Jonathan Squire** [2]

[1]Department of Physics and Astronomy, Queen Mary University of London, London E1 4NS, UK

[2]Physics Department, University of Otago, Dunedin 9010, New Zealand

(Received 1 June 2022; revised 23 August 2022; accepted 23 August 2022)

Weakly collisional plasmas are subject to nonlinear relaxation processes, which can operate at rates much faster than the particle collision frequencies. This causes the plasma to respond like a magnetised fluid despite having long particle mean free paths. In this Letter the effective collisional mechanisms are modelled in the plasma kinetic equation to produce density, pressure and magnetic-field responses to compare with spacecraft measurements of the solar wind compressive fluctuations at 1 AU. This enables a measurement of the effective mean free path of the solar wind protons, found to be $\approx 4 \times 10^5$ km, which is approximately 10^3 times shorter than the collisional mean free path. These measurements are shown to support the effective fluid behaviour of the solar wind at scales above the proton gyroradius and demonstrate that effective collision processes alter the thermodynamics and transport of weakly collisional plasmas.

Key words: space plasma physics, plasma properties

1. Introduction

Many natural plasmas (e.g. interstellar medium, galaxy clusters, black hole accretion disks, solar wind) are in a weakly collisional state, where the particle collision frequency $\nu_{\rm coll}$ is smaller than other characteristic frequencies (e.g. proton gyrofrequency $\Omega_{\rm p}$, inverse magnetic-field correlation time $1/\tau_c$ etc. (Quataert 2003; Marsch 2006; Schekochihin & Cowley 2006; Schekochihin *et al.* 2009). Thus, the regimes of the plasma motions, characterised by ω, can span from collisional (fluid) $\omega \ll \nu_{\rm coll}$ to collisionless $\omega \gg \nu_{\rm coll}$, where ω is the temporal frequency of a fluctuating plasma property (Schekochihin *et al.* 2005, 2009). Knowledge of the transition scale $\omega \sim \nu_{\rm coll}$ is vital to understand the behaviour of astrophysical plasmas.

The escaping solar corona, known as the solar wind, expands into interplanetary space as a super-Alfvénic and turbulent plasma (Parker 1958; Bruno & Carbone 2013; Verscharen, Klein & Maruca 2019). *In situ* measurements of particle distribution functions and electromagnetic fields enable fundamental plasma physics observations (Chen 2016). The Spitzer–Härm proton–proton collision frequency $\nu_{\rm p,p}^{\rm SH}$ decreases with radial distance

† Email address for correspondence: j.t.coburn@qmul.ac.uk

from the Sun and, by a few solar radii, is much smaller than other characteristic frequencies. In principle, the dynamics should be described by collisionless plasma equations. For reference, at 1 AU, typical frequencies are $\nu_{\mathrm{p,p}}^{\mathrm{SH}} \approx 4 \times 10^{-7}\ \mathrm{s}^{-1}$, $\Omega_{\mathrm{p}} \approx 10^{-1}\ \mathrm{s}^{-1}$, $1/\tau_c \approx 10^{-6}\ \mathrm{s}^{-1}$ (see Appendix A for the calculation of the collision frequency; Spitzer 1962; Huba 1983; Matthaeus *et al.* 2010; Verscharen *et al.* 2019).

Despite the weak collisionality of the solar wind, many aspects appear to be described by fluid equations: magnetohydrodynamic (MHD) turbulence theory predicts the shape of power spectra (e.g. magnetic field, proton density; Coleman 1968; Matthaeus & Goldstein 1982; Tu & Marsch 1995; Goldreich & Sridhar 1997; Bruno & Carbone 2013), spatial transport (Zank, Matthaeus & Smith 1996; Matthaeus *et al.* 1999) and the proton heating rate by the energy cascade (MacBride, Smith & Forman 2008; Stawarz *et al.* 2009; Coburn *et al.* 2012). This success is certainly due, in part, to the dominance of Alfvénic fluctuations, which have identical properties in the collisionless and fluid limits on scales above the proton gyroradius, implying much of the turbulent energy cascade is basically insensitive to the plasma's collisionality (Kulsrud, Sagdeev & Rosenbluth 1980; Schekochihin *et al.* 2009). However, observations show a strong correlation between the density and thermal pressure (i.e. compressive fluctuations), indicating a polytropic equation of state (Marsch *et al.* 1983; Totten, Freeman & Arya 1995; Verscharen, Chen & Wicks 2017; Nicolaou *et al.* 2020). Moreover, compressive fluctuations generally display the MHD slow-mode polarisation (anticorrelated magnetic and thermal pressure; Verscharen *et al.* 2017), rather than being severely damped, as expected in a collisionless plasma (Barnes 1966). These modes are routinely detected at a range of scales (Tu & Marsch 1995; Kellogg & Horbury 2005; Yao *et al.* 2011; Howes *et al.* 2012; Klein *et al.* 2012; Yao *et al.* 2013*a*,*b*) following a power law predicted from the MHD equations (Montgomery, Brown & Matthaeus 1987; Marsch & Tu 1990; Lithwick & Goldreich 2001; Schekochihin *et al.* 2009).

While the Spitzer–Härm collision frequency appears incompatible with the fluid-like behaviour of the solar wind, weakly collisional plasmas are also subject to collisionless relaxation processes that prevent extreme departure from equilibrium (Nishida 1969; Griffel & Davis 1969; Hamasaki & Krall 1973; Gary, Yin & Winske 2000; Yoon 2017). Solar wind observations present substantial evidence of temperature anisotropy instabilities constraining the particle distribution functions (Kasper, Lazarus & Gary 2002; Tu & Marsch 2002; Marsch 2006; Hellinger *et al.* 2006; Bale *et al.* 2009; Chen *et al.* 2016; Yoon 2017). These processes can play a similar role to collisions *viz.*, they are effective collision processes.

This Letter presents a measurement of the effective mean free path of the solar wind by comparing observations of compressive wave-mode polarisation with numerical solutions of varying effective collision frequency. It is shown that the transition from fluid to collisionless dynamics in the solar wind occurs at scales several orders of magnitude below the classical Spitzer–Härm mean free path, explaining the fluid-like behaviour of the weakly collisional solar wind.

2. Theory and numerical solutions

The kinetic MHD equations with the Bhatnagar–Gross–Krook (BGK) collision operator (Bhatnagar, Gross & Krook 1954; Gross & Krook 1956) produce dispersion relations and plasma fluctuations (e.g. magnetic field and pressure) that span between the collisionless and collisional limits (Kulsrud *et al.* 1980; Snyder, Hammett & Dorland 1997; Sharma, Hammett & Quataert 2003; Chandran *et al.* 2011). They describe a non-relativistic, magnetised plasma of arbitrary collision frequency (Kulsrud *et al.* 1980; Sharma *et al.*

https://doi.org/10.1017/S0022377822000836 Published online by Cambridge University Press

2003). See Appendix B for details on the equations and BGK collision operator. The specific equations, which we refer to as kinetic MHD-BGK (KMHD-BGK), model both the proton and electron responses with the kinetic equation so that Landau and Barnes dampings are retained. The BGK operator is used here to model relaxation processes, not particle collisions, so we use the language of an effective proton collision frequency $\nu_{\rm eff}$ or mean free path $\lambda^{\rm eff}_{\rm mfp} = v^{\rm p}_{\rm th}/\nu_{\rm eff}$, where the proton thermal speed is $v^{\rm p}_{\rm th}$.

Assuming plasma motions are slow compared with the gyrofrequency Ω_p, the second moment of the kinetic equation and the ideal induction equation leads to

$$n_{\rm p}B\frac{\rm d}{{\rm d}t}\left(\frac{p^{\rm p}_\perp}{n_{\rm p}B}\right) = -\boldsymbol{\nabla}\cdot(q^{\rm p}_\perp\hat{\boldsymbol{b}}) - q^{\rm p}_\perp\boldsymbol{\nabla}\cdot\hat{\boldsymbol{b}} + \frac{\nu_{\rm eff}}{3}(p^{\rm p}_\parallel - p^{\rm p}_\perp), \tag{2.1a}$$

$$\frac{n^3_{\rm p}}{2B}\frac{\rm d}{{\rm d}t}\left(\frac{p^{\rm p}_\parallel B^2}{n^3_{\rm p}}\right) = -\boldsymbol{\nabla}\cdot(q^{\rm p}_\parallel\hat{\boldsymbol{b}}) + q^{\rm p}_\perp\boldsymbol{\nabla}\cdot\hat{\boldsymbol{b}} + \frac{2\nu_{\rm eff}}{3}(p^{\rm p}_\perp - p^{\rm p}_\parallel), \tag{2.1b}$$

where ${\rm d}/{\rm d}t$ is the convective derivative and the quantities are the proton density $n_{\rm p}$, magnetic-field strength B, parallel (perpendicular) proton pressure $p^{\rm p}_\parallel$ ($p^{\rm p}_\perp$), field parallel flux of parallel (perpendicular) proton heat $q^{\rm p}_\parallel$ ($q^{\rm p}_\perp$) and the unit magnetic-field vector $\hat{\boldsymbol{b}} = \boldsymbol{B}/B$ (Chew, Goldberger & Low 1956; Hunana *et al.* 2019). The Alfvén speed is $v_A = B/\sqrt{4\pi n_{\rm p} m_{\rm p}}$, the proton gyroradius is $\rho_{\rm p} = v^{\rm p}_{\rm th}/\Omega_{\rm p}$ and the ion-acoustic speed is $c_{\rm s} = \sqrt{(3k_{\rm B}T^{\rm p}_\parallel + k_{\rm B}T^{\rm e}_\parallel)/m_{\rm p}}$, where the parallel proton (electron) temperature is $T^{\rm p}_\parallel(T^{\rm e}_\parallel)$.

Equations (2.1) are often discussed when the right-hand sides are zero and are then referred to as the double adiabatic equations or Chew–Goldberger–Low (CGL) invariants (Chew *et al.* 1956). The focus here is on how the CGL invariants are broken, for example, by the heat flux terms in the collisionless limit, and by the effective collisional terms ($\propto \nu_{\rm eff}$). Therefore, the relative non-conservation of the CGL invariants provides a sensitive test of the equation of state.

Cross-correlations and amplitude ratios, which can be measured, are constructed from the left-hand sides of (2.1),

$$C_\parallel = \frac{\langle \delta p^{\rm p}_\parallel\, \delta(n^3_{\rm p}/B^2)\rangle}{\langle|\delta p^{\rm p}_\parallel|^2\rangle^{1/2}\langle|\delta(n^3_{\rm p}/B^2)|^2\rangle^{1/2}}, \tag{2.2a}$$

$$A_\parallel = \frac{\langle|\delta(n^3_{\rm p}/B^2)|^2\rangle^{1/2}}{\langle n^3_{\rm p}/B^2\rangle}\frac{\langle p^{\rm p}_\parallel\rangle}{\langle|\delta p^{\rm p}_\parallel|^2\rangle^{1/2}}, \tag{2.2b}$$

$$C_\perp = \frac{\langle \delta p^{\rm p}_\perp\, \delta(n_{\rm p}B)\rangle}{\langle|\delta p^{\rm p}_\perp|^2\rangle^{1/2}\langle|\delta(n_{\rm p}B)|^2\rangle^{1/2}}, \tag{2.2c}$$

$$A_\perp = \frac{\langle|\delta(n_{\rm p}B)|^2\rangle^{1/2}}{\langle n_{\rm p}B\rangle}\frac{\langle p^{\rm p}_\perp\rangle}{\langle|\delta p^{\rm p}_\perp|^2\rangle^{1/2}}, \tag{2.2d}$$

where $\delta\chi = \chi - \langle\chi\rangle$ is the fluctuation about the average $\langle\chi\rangle$. They describe the relative non-conservation of the CGL invariants. The method compares predictions for (2.2) derived from the slow-mode eigenmodes of the linearised KMHD-BGK system (e.g. $\delta p^{\rm p}_\perp$, δB etc.) with solar wind measurements, since the slow mode is the dominant compressive mode at large scales (Howes *et al.* 2012). A description of the equations and the linear system of equations appears in Appendix B.

The model's free parameters are the propagation angle $\theta_{\hat{\boldsymbol{b}},\hat{\boldsymbol{k}}}$ and proton effective mean free path $\lambda^{\rm eff}_{\rm mfp}$; they are determined by fitting to solar wind observations. The wavenumber

https://doi.org/10.1017/S0022377822000836 Published online by Cambridge University Press

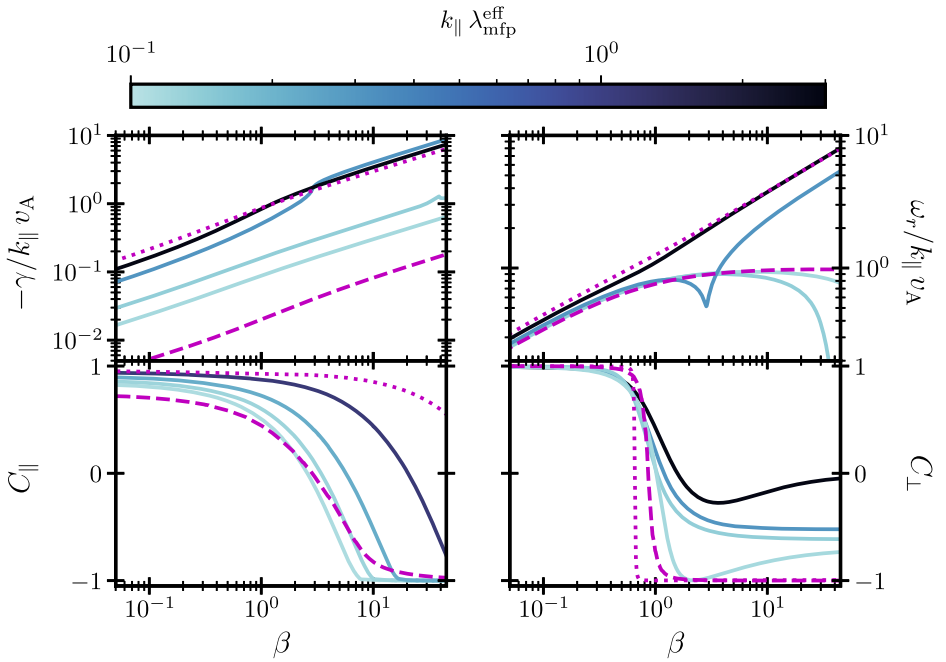

FIGURE 1. Numerical solutions of the KMHD-BGK equations for a range of $k_\parallel \lambda^{\rm eff}_{\rm mfp}$ (see colour bar). The imaginary (real) part of the complex frequency is denoted γ (ω_r). The dotted (dashed) magenta lines are the long (short) limit of $\lambda^{\rm eff}_{\rm mfp}$ corresponding to the collisionless (collisional) slow-mode/ion-acoustic branch for $\theta_{\hat{\boldsymbol{b}},\hat{\boldsymbol{k}}} = 88^\circ$ (Howes *et al.* 2006; Verscharen *et al.* 2017).

k and the proton beta $\beta = 8\pi p^{\rm p}/B^2$, where $p^{\rm p} = 2p^{\rm p}_\perp/3 + p^{\rm p}_\parallel/3$, are set to measured values. The species temperature ratio is set to a typical value for the solar wind $T_{\rm p}/T_{\rm e} = 1$ and the effective mean free path species ratio is set to $\lambda^{\rm eff}_{\rm mfp}/\lambda^{\rm eff}_{\rm mfp,electrons} = 1$ (see Appendix B for details). At small β, these two ratios $T_{\rm p}/T_{\rm e}$, $\lambda^{\rm eff}_{\rm mfp}/\lambda^{\rm eff}_{\rm mfp,electrons}$ have an insignificant influence on the correlations, (2.2), and nearly no influence at large β.

Figure 1 demonstrates the ability of the KMHD-BGK equations to resolve the dynamics of the compressive slow mode from collisional (lighter blue) to collisionless (black). Numerical predictions for (2.2*a*), (2.2*c*) (bottom panels of figure 1) show distinct differences at $\beta > 1$ for different $k_\parallel \lambda^{\rm eff}_{\rm mfp}$, which can be compared with observations. The MHD ($k_\parallel \lambda^{\rm eff}_{\rm mfp} \ll 1$) and collisionless ($k_\parallel \lambda^{\rm eff}_{\rm mfp} \gg 1$) limits are illustrated in magenta, for $C_\perp$ (bottom right panel) these two limits produce similar trends, therefore it is necessary to make comparisons at multiple $k_\parallel$ to measure $\lambda^{\rm eff}_{\rm mfp}$.

3. Measurements

The dataset consists of Wind spacecraft measurements of the pristine solar wind during years 2005–2010. The electrostatic analyser, 3DP, records onboard moments of the proton density, velocity and pressure tensor, and the magnetometer MFI records the magnetic field, at a nominal $\sim 3s$ cadence (Lepping *et al.* 1995; Lin *et al.* 1995).

The dataset is restricted to time intervals satisfying three criteria: (i) 95 % of the data are available (the remaining are then linearly interpolated); (ii) the median density must be greater than 1 particle per cm^3; and (iii) the average norm of the non-gyrotropic tensor ($\boldsymbol{\Pi}^{\rm p} = \mathsf{p}^{\rm p} - \hat{\boldsymbol{b}}\hat{\boldsymbol{b}}\, p^{\rm p}_\parallel - (1 - \hat{\boldsymbol{b}}\hat{\boldsymbol{b}})p^{\rm p}_\perp$), must be less than 30 % of the average norm of the

https://doi.org/10.1017/S0022377822000836 Published online by Cambridge University Press

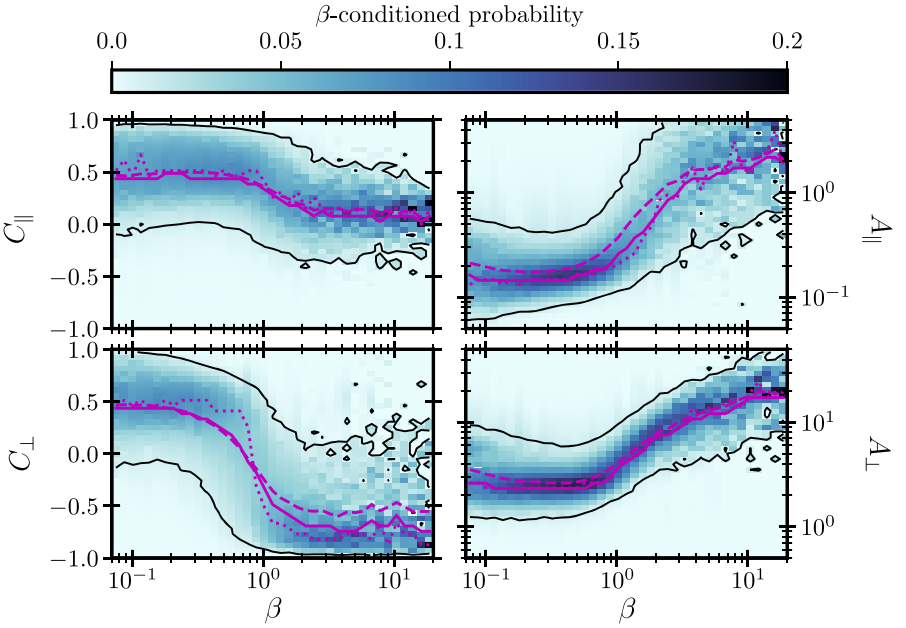

FIGURE 2. The β-conditioned probability functions of the quantities in (2.2) for the wavenumber bin $k_{\rm SW} = 0.288 \times 10^{-5}$ km^{-1}. The thin black line is a contour of probability equal to 0.01. The magenta lines are mean (dashed), median (solid) and maximum (dotted) conditioned on β.

pressure tensor $\mathsf{p}^{\rm p}$. The final point here is satisfied ∼94 % of the time at the ∼3s time interval and more so at longer time intervals.

To probe a set of wavenumbers, the four quantities in (2.2) are measured, along with the average radial solar wind velocity $\langle V_{\rm SW}\rangle$ and the average proton beta for a set of time intervals $\tau = [30\ \text{s}, 1\ \text{min.}, 2\ \text{mins.}, \ldots, 128\ \text{mins.}]$. The time scales are converted to wavenumber $k_{\rm SW} = 1/\tau\langle V_{\rm SW}\rangle$ via Taylor's frozen-in-flow (TFF) assumption (Taylor 1938). Outliers in the distribution of $k_{\rm SW}$ are removed and then three bins of equal probability density are obtained where the median of each bin is $k_{\rm SW} = [0.288, 1.41, 6.34] \times 10^{-5}$ km^{-1}, which lies within the inertial range of the magnetic-field power spectrum at 1 AU (Kiyani, Osman & Chapman 2015). The choice of bins provides enough separation in wavenumber to resolve differences in the measured quantities (e.g. figure 1) and sufficient sampling; the wavenumber bins contain $[2.98, 16.6, 70.0] \times 10^5$ samples.

For bin $k_{\rm SW} = 0.288 \times 10^{-5}$ km^{-1} the β-conditioned probability functions of (2.2), mapped to a common colour bar, are displayed in figure 2. The β-trend lines in magenta (see caption) capture statistically significant differences between $\beta \lessgtr 1$. From the correlations $C_\parallel, C_\perp$ it is clear that the CGL invariants are rarely conserved ($C_\parallel, C_\perp = 1$), but display similar trends to the theoretical expectations seen in figure 1. The amplitude ratios $A_\parallel, A_\perp$ demonstrate a relative decrease in fluctuation amplitude of the pressure components at $\beta > 1$.

4. Comparison of measurements and numerical solutions

The theoretical predictions for (2.2) from the numerical model in § 2 are compared with the observations in figure 2 to determine the most probable effective mean free path $\lambda_{\rm mfp}^{\rm eff}$

https://doi.org/10.1017/S0022377822000836 Published online by Cambridge University Press

and propagation angles $\theta_{\hat{\boldsymbol{b}},\hat{\boldsymbol{k}}}$. The numerical predictions can be fitted to the observations by altering the parameters (e.g. the effective mean free path), but a degeneracy in parametrisation must be dealt with. The numerical solutions primarily depend on $k_\parallel \lambda_{\mathrm{mfp}}^{\mathrm{eff}} = k\cos(\theta_{\hat{\boldsymbol{b}},\hat{\boldsymbol{k}}})\lambda_{\mathrm{mfp}}^{\mathrm{eff}}$ (Sharma *et al.* 2003), which implies that $\lambda_{\mathrm{mfp}}^{\mathrm{eff}}$ and $\theta_{\hat{\boldsymbol{b}},\hat{\boldsymbol{k}}}$ are degenerate. To address this, a scale-dependent anisotropy model ($k_\parallel \sim k_\perp^\alpha$) is introduced, which relates k and $\theta_{\hat{\boldsymbol{b}},\hat{\boldsymbol{k}}}$,

$$k = \frac{k_{\mathrm{iso}}}{\sqrt{2}}\left[\sin\left(\theta_{\hat{\boldsymbol{b}},\hat{\boldsymbol{k}}}\right)\right]^{\alpha/(1-\alpha)}\left[\cos\left(\theta_{\hat{\boldsymbol{b}},\hat{\boldsymbol{k}}}\right)\right]^{1/(\alpha-1)}, \tag{4.1}$$

where k_{iso} is the isotropic wavenumber ($k = k_{\mathrm{iso}}$ when $k_\perp = k_\parallel$) and α is the anisotropy exponent, generalised from turbulence models (Goldreich & Sridhar 1995). The wavenumber model provides $\theta_{\hat{\boldsymbol{b}},\hat{\boldsymbol{k}}}$, given k, parameterised by α, k_{iso}, so that $\lambda_{\mathrm{mfp}}^{\mathrm{eff}}$ can be determined at the given wavenumber. Then comparing solutions parameterised by $\lambda_{\mathrm{mfp}}^{\mathrm{eff}}$, α, k_{iso} at multiple wavenumbers $k = k_{\mathrm{SW}}$ clears the degeneracy and allows all three parameters to be measured. Additionally, the model permits quantification of the observed increase of obliqueness with wavenumber of the compressive fluctuations (Chen *et al.* 2012; Chen 2016).

Finally, the predictions of (2.2) from the numerical solutions are normalised to the measured β-conditioned mean value (dashed magenta lines in figure 2) of $C_\parallel, C_\perp, A_\parallel, A_\perp$ at $\beta \simeq 10^{-1}$. This is to account for the fact that linear wave properties are only approximately observed in strong turbulence (Chen 2016; Grošelj *et al.* 2019).

The ranges $\alpha = [0.05, 1.0]$, $k_{\mathrm{iso}} = [5\times10^{-9}, 5\times10^{-7}]$ km^{-1} and $\lambda_{\mathrm{mfp}}^{\mathrm{eff}} = [3.5\times10^{4}, 2.1\times10^{6}]$ km are chosen for computing numerical solutions. The ranges of α, k_{iso} are consistent with previous observations (Chen *et al.* 2012; Chen 2016). The range of $\lambda_{\mathrm{mfp}}^{\mathrm{eff}}$ returns numerical solutions of (2.2) that compare qualitatively well with the observations (seen in figure 2). The Spitzer–Härm mean free path returns the (collisionless) ion-acoustic dispersion relation which is inconsistent with the measurements.

To make a quantitative comparison, we compute the 'goodness of fit'

$$R = \sqrt{N^{-1}\sum_{i}^{N}(\bar{y}_i - \hat{y}_i)^2}, \tag{4.2}$$

where $\hat{y}_i$ ($\bar{y}_i$) is the local numerical solution (local measured mean), summed over i, denoting the ith β-bin. Here, $R(k_{\mathrm{SW}};\alpha,k_{\mathrm{iso}},\lambda_{\mathrm{mfp}}^{\mathrm{eff}})$ is calculated for each wavenumber k_{SW}, where the mean $\bar{y}_i$ is respective to the wavenumber bin. The R-values are inverted for unnormalised weights ($w = R^{-1}$), divided by the maximum weight (w_{max}), then summed over wavenumber $\mathcal{W}(\alpha,k_{\mathrm{iso}},\lambda_{\mathrm{mfp}}^{\mathrm{eff}}) = \sum_k w(k;\alpha,k_{\mathrm{iso}},\lambda_{\mathrm{mfp}}^{\mathrm{eff}})/w_{\mathrm{max}}$ to break the aforementioned degeneracy. From this volume, weighted geometric means μ_x, covariances $\sigma_{x,y}^2$, and two sigma confidence intervals CI_x are calculated (see Appendix C for the statistics; Norris 1940; Kendall & Stuart 1977). This is the method employed to measure the quantities $\lambda_{\mathrm{mfp}}^{\mathrm{eff}}$, α, k_{iso}, providing the main results of the Letter.

To visualise the weighted parameter space for $C_\perp$, figure 3 illustrates the weight volume $\mathcal{W}(\alpha,k_{\mathrm{iso}},\lambda_{\mathrm{mfp}}^{\mathrm{eff}})$ numerically integrated over each parameter axis χ,

$$\mathcal{W}_\chi = \int_{\chi_0}^{\chi_n} \mathrm{d}\chi\, \frac{\mathcal{W}(\alpha,k_{\mathrm{iso}},\lambda_{\mathrm{mfp}}^{\mathrm{eff}})}{\chi_n - \chi_0}, \tag{4.3}$$

where χ_n, χ_0 are limits of the range. The weighted means in figure 3 lie in the maximum regions of $\mathcal{W}_\chi$, within the confidence intervals, indicating the weighted geometric statistics are a good representation of the observations.

https://doi.org/10.1017/S0022377822000836 Published online by Cambridge University Press

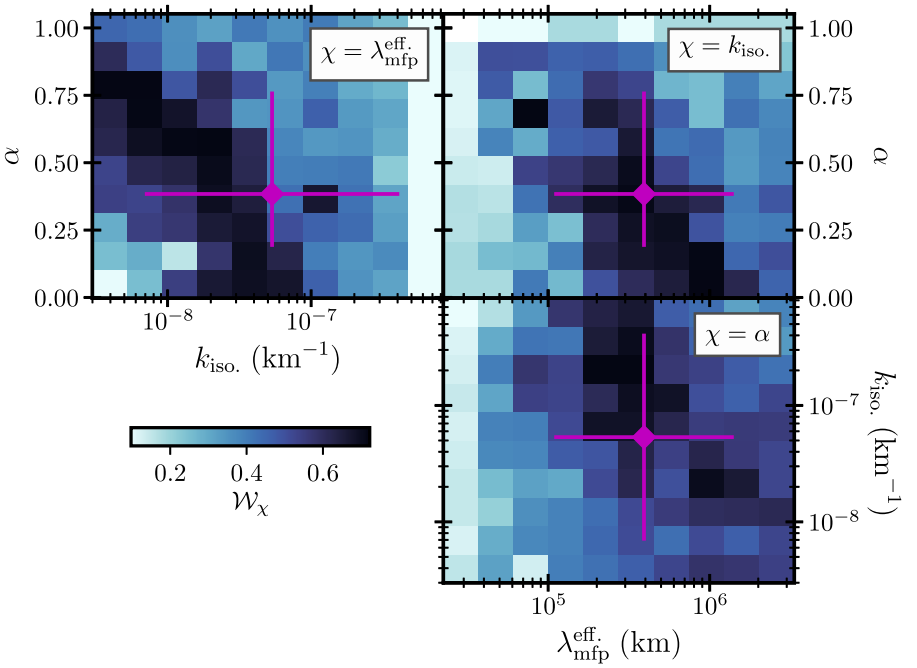

FIGURE 3. The three panels display the integrated weight volume, (4.3), for each parameter χ, for $C_\perp$. The magenta crosses indicate the weighted geometric means and two sigma confidence intervals.

To check the scale dependence, figure 4 displays the observed β-conditioned means of (2.2) and the numerical solutions corresponding to the maximum $\mathcal{W}$. The numerical solutions and observations trend similarly with wavenumber, indicating the scale dependence of the effective collisionality has been well modelled. The parameters of the maximum (recorded in figure 4) do not correspond exactly to the weighted geometric means of $\mathcal{W}$ (seen in figure 3), reflecting the statistical nature of the measured quantities.

The method of calculating statistics for $\lambda^{\rm eff}_{\rm mfp}, \alpha, k_{\rm iso}$ displayed in figure 3 for $C_\perp$ produces similar statistics for $C_\parallel, A_\parallel, A_\perp$ (see Appendix C). Therefore, in table 1, combined statistics are reported. The measured effective mean-free-path and mean proton thermal speed (measured with this dataset) give an effective collision frequency of $\nu_{\rm eff} = v^{\rm p}_{\rm th}/\lambda^{\rm eff}_{\rm mfp} = 1.11 \times 10^{-4}$ s^{-1}.

The transition frequency, where $\nu_{\rm eff} \simeq \omega$, can be estimated with $\nu_{\rm eff}$ and the ion-acoustic dispersion relation $\omega_{\rm IA} = k_\parallel c_{\rm s}$, giving the parallel transition wavenumber $k^{\rm trans}_\parallel = v^{\rm p}_{\rm th}/c_{\rm s}\, \lambda^{\rm eff}_{\rm mfp}$. Using the wavenumber model, (4.1), the transition wavenumber is

$$k^{\rm trans} = \frac{v^{\rm p}_{\rm th}}{c_{\rm s}\, \lambda^{\rm eff}_{\rm mfp}} \sqrt{1 + \left[\frac{2\left(v^{\rm p}_{\rm th}\right)^2}{\left(\lambda^{\rm eff}_{\rm mfp}\, k_{\rm iso}\, c_{\rm s}\right)^2}\right]^{(1-\alpha)/\alpha}} \tag{4.4}$$

(more details are provided in Appendix D). Inserting the combined statistics from table 1, using a typical value of $v^{\rm p}_{\rm th}/c_{\rm s} = \sqrt{1/2}$ for the solar wind, and using the TFF assumption, the transition wavenumber in spacecraft-frame frequency at 1 AU is $\langle V_{\rm SW}\rangle\, k^{\rm trans} = f^{\rm trans} = 0.19$ Hz and $\mathrm{CI}_{f^{\rm trans}} = [0.046, 0.33]$ Hz. The uncertainties are propagated from $V_{\rm SW}$ and the four estimates of $k^{\rm trans}$ from $C_\parallel,\ A_\parallel,\ C_\perp,\ A_\perp$.

https://doi.org/10.1017/S0022377822000836 Published online by Cambridge University Press

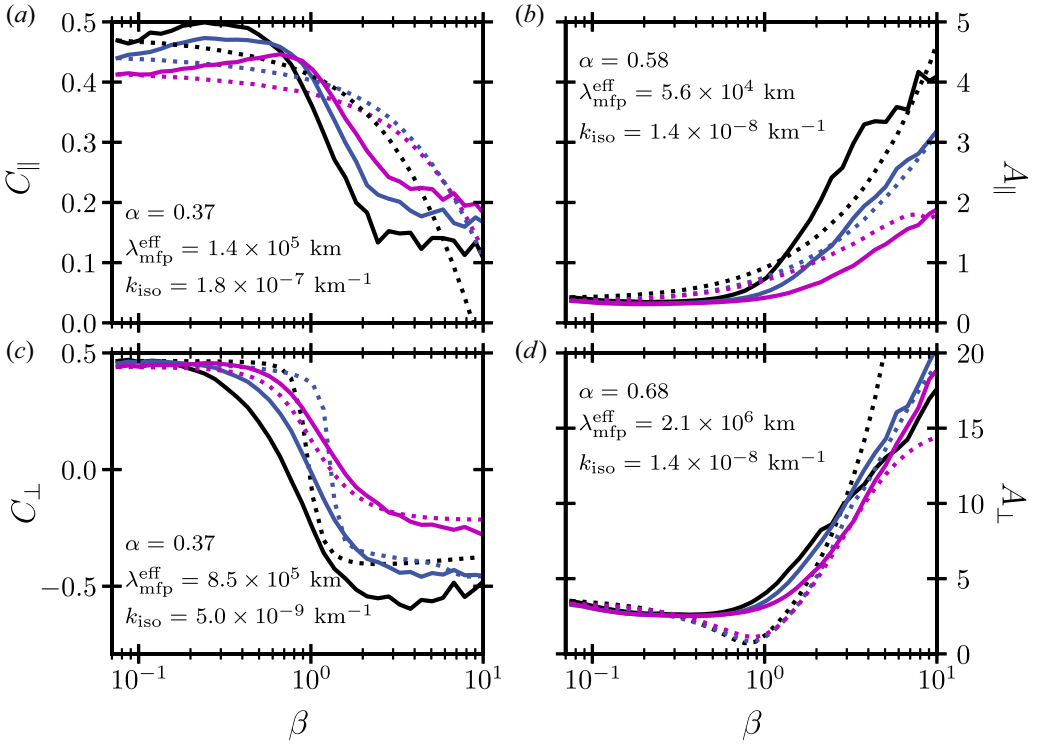

FIGURE 4. The panels (*a–d*) show the β-conditioned mean of the four quantities in (2.2) for the three median wavenumber bins $k_{\rm SW} = [0.288, 1.41, 6.34] \times 10^{-5}$ km^{-1} as solid (black, blue, magenta) lines, respectively. Statistical uncertainties on the mean trends can be seen in figure 2. The dashed lines are the numerical solutions corresponding to the maximum $\mathcal{W}$; the parameters of the maximum are reported in the panels.

Statistic	Value(s)	Unit
μ_α	0.43	—
$\mu_{k_{\rm iso}}$	5.4×10^{-8}	km^{-1}
$\mu_{\lambda_{\rm mfp}^{\rm eff}}$	4.4×10^5	km
${\rm CI}_\alpha$	[0.21, 0.86]	—
${\rm CI}_{k_{\rm iso}}$	$[0.064, 4.5] \times 10^{-7}$	km^{-1}
${\rm CI}_{\lambda_{\rm mfp}^{\rm eff}}$	$[0.10, 19] \times 10^5$	km
$\sigma^2_{\alpha,k_{\rm iso}}/(\sigma_{\alpha,\alpha}\,\sigma_{k_{\rm iso},k_{\rm iso}})$	0.22	—
$\sigma^2_{\alpha,\lambda_{\rm mfp}^{\rm eff}}/(\sigma_{\alpha,\alpha}\,\sigma_{\lambda_{\rm mfp}^{\rm eff},\lambda_{\rm mfp}^{\rm eff}})$	0.34	—
$\sigma^2_{k_{\rm iso},\lambda_{\rm mfp}^{\rm eff}}/(\sigma_{k_{\rm iso},k_{\rm iso}}\sigma_{\lambda_{\rm mfp}^{\rm eff},\lambda_{\rm mfp}^{\rm eff}})$	0.17	—

TABLE 1. Combined weighted geometric mean μ_x, standard deviation $\sigma_{x,x}$ and the two sigma confidence interval ${\rm CI}_x$.

https://doi.org/10.1017/S0022377822000836 Published online by Cambridge University Press

5. Discussion

The relative non-conservation of the CGL invariants has been measured and the behaviour has been modelled with the slow-mode branch of the KMHD-BGK equations to measure the effective mean free path of the solar wind protons and the scale dependence of the slow-mode wavenumber anisotropy (table 1 reports the statistics of these measurements). The primary result of this Letter is the measured effective proton mean free path, which is $\sim 10^3$ times smaller than the Spitzer–Härm mean free path ($\lambda_{\mathrm{mfp}}^{\mathrm{SH}} = 1.14 \times 10^8$ km, see Appendix A). Therefore, the fluid-like range in the solar wind extends to much smaller scales than the prediction based on particle collisions. In addition, the scale-dependent anisotropy of the compressive fluctuations ($\alpha \simeq 0.4$) is consistent with previous measurements (Chen *et al.* 2012; Chen 2016), being more anisotropic than the Alfvénic fluctuations, which follow the critical balance value $\alpha_{\mathrm{CB}} = 2/3$ (Goldreich & Sridhar 1997).

The measured transition frequency, the scale between fluid behaviour ($f \ll f^{\mathrm{trans}}$) and collisionless behaviour ($f \gg f^{\mathrm{trans}}$), of $f^{\mathrm{trans}} = 0.19$ Hz is at the well-known break in power law ($k_\perp \rho_{\mathrm{p}} \sim 1$) of the magnetic-field power spectrum at 1 AU (Leamon *et al.* 1998; Kiyani *et al.* 2015; Verscharen *et al.* 2019). These measurements therefore justify the use of fluid MHD theory at larger scales ($k_\perp \rho_{\mathrm{p}} < 1$) (Tu & Marsch 1995; Goldreich & Sridhar 1997; Bruno & Carbone 2013; Chen 2016). If the result $k_\perp \rho_{\mathrm{p}} \simeq k_\parallel \lambda_{\mathrm{mfp}}^{\mathrm{eff}}$ turns out to be a general property of weakly collisional plasma, this provides a simple parameterisation for the effective collisionality of astrophysical plasmas.

The method employed in this Letter relies on linear theory to describe cross-correlations and amplitude ratios of various plasma properties. While there is evidence that such linear quantities are approximately preserved in solar wind turbulence (e.g. Chen 2016; Verscharen *et al.* 2017; Grošelj *et al.* 2019), and the numerical predictions in this Letter match the observations well, it would be interesting to study in the future the degree to which nonlinear effects may also contribute to these correlations. The BGK operator has been used in this work as a simple way to model effective collision processes, however, it is possible that the use of alternative collision operators may alter the numerical value of the effective mean free path obtained, although we would expect the order of magnitude result to hold. It should also be noted that the transition scale obtained here is consistent with previous observations of fluid-like behaviour in the solar wind above the ion gyroscale (Verscharen *et al.* 2017).

An important neglected effect is heating, which is needed to describe the solar wind temperature profile (Verma, Roberts & Goldstein 1995; Vasquez *et al.* 2007). Heating would also break the CGL invariants through additional terms appearing on the right-hand side of (2.1) (Chandran *et al.* 2011; Hellinger *et al.* 2013). The importance of this simplification can be addressed by comparing our measured effective collision time with the heating time inferred in previous papers (Vasquez *et al.* 2007; Hellinger *et al.* 2013). The heating time can be estimated from $Q_{\mathrm{heat}}/k_{\mathrm{B}}T_{\mathrm{p}} = \nu^{\mathrm{heat}} \approx 10^{-6}\ \mathrm{s}^{-1}$, which is approximately 10^2 times smaller than the effective collision frequency (ν_{eff}) measured in this Letter. This suggests isotropisation dominates over heating, which is not unreasonable given the extreme anisotropic evolution the CGL invariants would dictate due to expansion ($T_\perp^{\mathrm{p}} \propto R^{-2}$, $T_\parallel^{\mathrm{p}} \propto$ const., where R is the radial distance from the Sun; Matteini *et al.* 2012).

There are many possible mechanisms that could lead to the observed effective collision frequency. It is well known that large departures from the Maxwellian velocity distribution function invalidate the Spitzer–Härm approach (Marsch 2006), in particular, large gradients in velocity space lead to fast collisional thermalisation (Pezzi, Valentini & Veltri 2016). However, given that the departure from Spitzer–Härm is a factor $\approx 10^3$,

https://doi.org/10.1017/S0022377822000836 Published online by Cambridge University Press

and the fact that our analysis is based on the properties of the low-order moments of the velocity distribution function (which would not be strongly influenced by collisional effects; Pezzi *et al.* 2019), collisional processes are very unlikely to lead to the observed behaviour, implicating collisionless physics.

Previous works have suggested a range of possible effective collision processes that can arise in collisionless plasmas. These include wave–particle interactions (Kellogg 2000; Graham *et al.* 2022), instabilities (Gary *et al.* 2000; Yoon 2017) and the plasma wave echo (Schekochihin *et al.* 2016; Meyrand *et al.* 2019). They have long been studied theoretically and numerically (Coroniti & Eviatar 1977; Schekochihin & Cowley 2006; Kunz, Schekochihin & Stone 2014; Helander, Strumik & Schekochihin 2016; Kunz, Stone & Quataert 2016; Rincon *et al.* 2016; Squire, Quataert & Kunz 2017), but it is an open question as to the relevant role of the various mechanisms and how they are activated (Verscharen *et al.* 2016; Squire *et al.* 2017; Kunz *et al.* 2020). Therefore, further studies are necessary to assess exactly what key physics of a weakly collisional plasma leads to the measured effective collisionality, since most astrophysical plasmas, being multi-scale and turbulent, will support effective collision mechanisms (Zhuravleva *et al.* 2019). The measurements presented here provide constraints to be satisfied by theories of effective collision processes.

Acknowledgements

We would like to thank S.D. Bale for pointing us to the dataset and L.B. Wilson III for helping us understand the dataset.

Editor Thierry Passot thanks the referees for their advice in evaluating this article.

Funding

J.T.C. was supported by a QMUL Principal Studentship. C.H.K.C. was supported by UKRI Future Leaders Fellowship MR/W007657/1, STFC Ernest Rutherford Fellowship ST/N003748/2, and STFC Consolidated Grant ST/T00018X/1. Support for J.S. was provided by Rutherford Discovery Fellowship RDF-U001804, which is managed through the Royal Society Te Apārangi.

Declaration of interests

The authors report no conflict of interest.

Appendix A. Collision length and time scales

Following the unit convention of Huba (1983), the Spitzer–Härm proton–proton collision frequency (Spitzer 1962) for a proton–electron plasma with $T_\mathrm{p} \leqslant T_\mathrm{e}$, where T_p (T_e) is the proton (electron) temperature, is written

$$\nu_{\mathrm{p,p}}^{\mathrm{SH}} = 4.8 \times 10^{-8}\, n_\mathrm{p} (k_\mathrm{B} T_\mathrm{p})^{-3/2}\, \lambda \left(\mathrm{s}^{-1}\right), \tag{A1}$$

where n_p (cm^{-3}) is the proton number density, $k_\mathrm{B}\, T_\mathrm{p}$ is in eV and the Coulomb logarithm is λ. The Coulomb logarithm for proton–proton collisions

$$\lambda = 23 - \ln \left| \frac{\sqrt{2 n_\mathrm{p}}}{T_\mathrm{p}^{3/2}} \right|. \tag{A2}$$

https://doi.org/10.1017/S0022377822000836 Published online by Cambridge University Press

The dataset described in § 3 provides the following averages:

$$n_{\mathrm{p}} = 5.33\,(\mathrm{cm}^{-3}), \tag{A3}$$

$$k_{\mathrm{B}} T_{\mathrm{p}} = 30.0\,(\mathrm{eV}), \tag{A4}$$

$$v_{\mathrm{th}}^{\mathrm{p}} = 48.3\,(\mathrm{km/s}), \tag{A5}$$

where the proton thermal speed is $v_{\mathrm{th}}^{\mathrm{p}}$. With these measurements collision scales can be calculated

$$\nu_{\mathrm{p,p}}^{\mathrm{SH}} = 4.23 \times 10^{-7}\,(\mathrm{s}^{-1}), \tag{A6}$$

$$\lambda_{\mathrm{mfp}}^{\mathrm{SH}} = v_{\mathrm{th}}^{\mathrm{p}} / \nu_{\mathrm{p,p}}^{\mathrm{SH}} = 1.14 \times 10^{8}\,(\mathrm{km}), \tag{A7}$$

where $\lambda_{\mathrm{mfp}}^{\mathrm{SH}}$ is the Spitzer–Härm proton–proton mean free path.

Appendix B. Linear collisional-kinetic MHD

The kinetic magnetohydrodynamic (KMHD) equations are found in Kulsrud *et al.* (1980) where a BGK collision operator can be added (Snyder *et al.* 1997) to study wave modes of arbitrary collision frequency (Sharma *et al.* 2003). The BGK collision operator is defined as

$$\mathcal{C}_{\mathrm{BGK}}\big[F_s(\boldsymbol{v}; n_s, T_s), f_s(t, \boldsymbol{x}, \boldsymbol{v})\big] = \nu^s\big[F_s(\boldsymbol{v}; n_s, T_s) - f_s(t, \boldsymbol{x}, \boldsymbol{v})\big], \tag{B1}$$

where F_s is the equilibrium distribution function, assumed to be a Maxwellian, parameterised by the density (n_s) and temperature (T_s) to conserve particle number and energy. The BGK collision operator approximates any process that restores the distribution function (f_s) to the equilibrium (F_s) at a rate of ν^s.

The so-called drift kinetic equation is derived by transforming into the bulk velocity frame and assuming the distribution function is gyrotropic so the background electric can be ignored (Kulsrud *et al.* 1980). The equations are linearised on a static background and Fourier transformed to produce

$$\omega\tilde{u}_{\perp} + \frac{1}{\beta}\left(-k_{\perp}\tilde{b}_{\parallel} + k_{\parallel}\tilde{b}_{\perp}\right) - \frac{k_{\perp}}{2\beta}\left(\tilde{p}_{\perp}^{p} + \tilde{p}_{\perp}^{e}\right) = 0, \tag{B2}$$

$$\omega\tilde{u}_{\parallel} - \frac{k_{\parallel}}{2\beta}\tilde{p}_{\parallel} = 0, \tag{B3}$$

$$\omega\tilde{b}_{\perp} + k_{\parallel}\tilde{u}_{\perp} = 0, \tag{B4}$$

$$\omega\tilde{b}_{\parallel} - k_{\perp}\tilde{u}_{\perp} = 0, \tag{B5}$$

$$\omega\tilde{n} - \left(k_{\parallel}\tilde{u}_{\parallel} + k_{\perp}\tilde{u}_{\perp}\right) = 0, \tag{B6}$$

where ω is the complex frequency, $\tilde{u}_{\perp}$ ($\tilde{u}_{\parallel}$) is the perpendicular (parallel) bulk velocity, $k_{\perp}$ ($k_{\parallel}$) is the perpendicular (parallel) wavenumber, β is the proton beta, $\tilde{b}_{\perp}$ ($\tilde{b}_{\parallel}$) is the perpendicular (parallel) magnetic field, $\tilde{p}_{\perp}^{s}$ ($\tilde{p}_{\parallel}^{s}$) is the perpendicular (parallel) species 's' pressure and $\tilde{n}$ is the density (quasi-neutrality). The tilde denotes the Fourier amplitude. The equations are closed by taking density and pressure moments of the linear Fourier

https://doi.org/10.1017/S0022377822000836 Published online by Cambridge University Press

analysed drift kinetic equation, which produces

$$\tilde{n}\left(1+\zeta_\nu^s\,\mathcal{Z}^s\right)-\frac{\tilde{p}_\perp^s}{\beta_s}\left(1+\frac{2}{3}\zeta_\nu^s\,\mathcal{Z}^s\right)-\tilde{b}_\parallel\zeta_\omega^s\,\mathcal{Z}^s-\frac{\tilde{p}_\parallel^s}{\beta_s}\zeta_\nu^s\,\mathcal{Z}^s\frac{1}{3}=0 \tag{B7}$$

$$\begin{aligned}\tilde{n}\left[1+2(\zeta^s)^2\mathcal{R}^s+\frac{3}{2}\zeta_\nu^s\left(\mathcal{Z}^s-2\zeta^s\mathcal{R}^s\right)\right]-\frac{\tilde{p}_\parallel^s}{\beta_s}\left[\mathcal{R}^s+\frac{1}{6}\zeta_\nu^s\left(\mathcal{Z}^s-2\zeta^s\mathcal{R}^s\right)\right]\\ -\tilde{b}_\parallel\left[1+2(\zeta^s)^2\mathcal{R}^s-\mathcal{R}^s+\zeta_\nu^s\left(\mathcal{Z}^s-2\zeta^s\mathcal{R}^s\right)\right]-\frac{\tilde{p}_\perp^s}{\beta_s}\frac{1}{3}\zeta_\nu^s\left(\mathcal{Z}^s-2\zeta^s\mathcal{R}^s\right)=0,\end{aligned} \tag{B8}$$

with the definitions

$$\zeta_\omega^s=\frac{\omega}{|k_\parallel|v_{\mathrm{th}}^s},\quad \zeta_\nu^s=\frac{i\nu^s}{|k_\parallel|v_{\mathrm{th}}^s},\quad \zeta^s=\zeta_\omega^s+\zeta_\nu^s \tag{B9}$$

and $\mathcal{R}^s=1+\zeta^s\mathcal{Z}^s$. The plasma dispersion function is $\mathcal{Z}^s$ (Fried & Conte 2015). Throughout the text β is the proton beta and β_{e} is the electron beta. The kinetic equation for the electrons must be solved since the electron pressure appears in the momentum equation. The parameters relevant to the electrons are $T_{\mathrm{p}}/T_{\mathrm{e}}$ which is set to 1 and the effective mean free path species ratio $\lambda_{\mathrm{mfp}}^{\mathrm{eff}}/\lambda_{\mathrm{mfp,electrons}}$ which is set to 1, where the mean free path of the electrons is $\lambda_{\mathrm{mfp,electrons}}$. These equations form a linear system of equations that can be solved numerically and provide all the numerical solutions of the Letter.

Appendix C. Weighted geometric statistics

This appendix follows Norris (1940); Kendall & Stuart (1977). If the observations x_i have unnormalised weights w_i, the definitions follow of the weighted geometric mean

$$\mu^x=\exp\left\{\sum_i^n\frac{w_i\ln|x_i|}{\sum_i^n w_i}\right\}, \tag{C1}$$

weighted geometric covariance matrix

$$\left(\sigma^{x,y}\right)^2=\exp\left\{\frac{1}{\sum_i^n w_i}\sum_i^n w_i\ln\left|\frac{x_i}{\mu^x}\right|\ln\left|\frac{y_i}{\mu^y}\right|\right\}, \tag{C2}$$

and the two sigma standard deviation

$$\ln|\mu^x|\pm 2\ln|(\sigma^{x,x})|\;\Rightarrow\;\mathrm{CI}^x=[\mu^x\,(\sigma^{x,x})^2,\;\mu^x/(\sigma^{x,x})^2], \tag{C3}$$

where CI^x is the weighted geometric confidence interval. The statistics detailed here are used to calculate the main results of the Letter, which are reported in table 1.

Figure 5 shows that the statistics of $\alpha, k_{\mathrm{iso}}, \lambda_{\mathrm{mfp}}^{\mathrm{eff}}$ for $C_\perp, C_\parallel, A_\perp, A_\parallel$ are similar so that combined statistics are reported in table 1. Figure 5(*b*,*d*,*f*) shows the normalised weighted geometric covariance between the model parameters

$$\left(\hat{\sigma}^{x,y}\right)^2=\frac{\left(\sigma^{x,y}\right)^2}{\sigma^{x,x}\,\sigma^{y,y}}. \tag{C4}$$

These terms are small.

https://doi.org/10.1017/S0022377822000836 Published online by Cambridge University Press

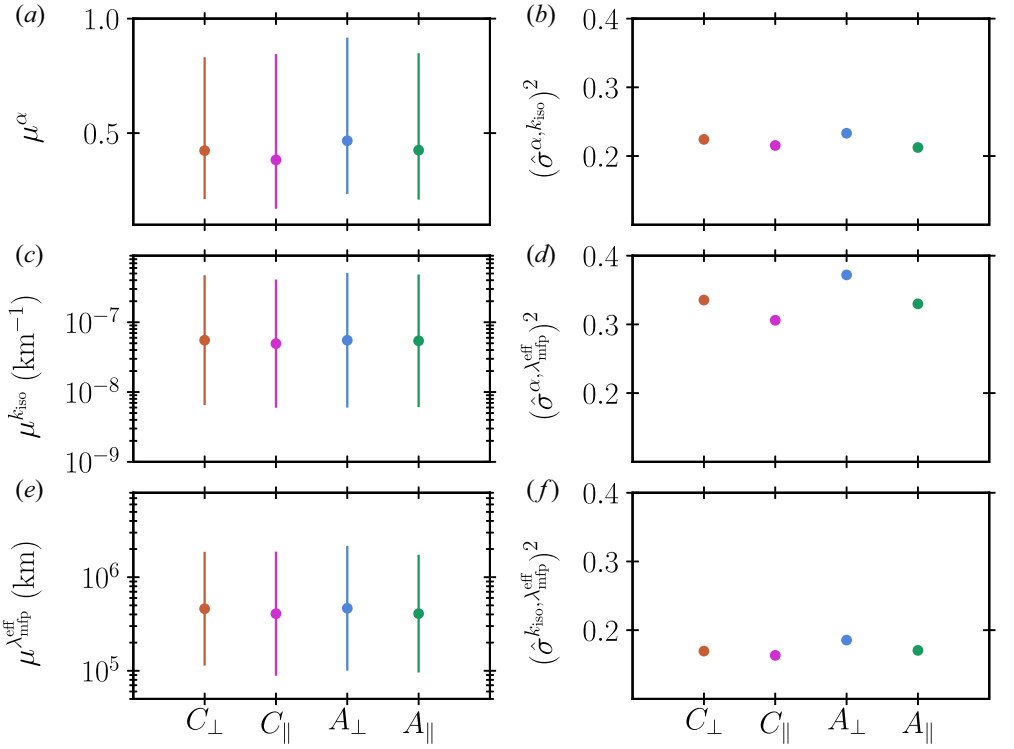

FIGURE 5. The weighted geometric means, (C1), are plotted in (*a*,*c*,*e*) as circles and the confidence intervals, (C3), are plotted as a vertical lines. Panels (*b*,*d*,*f*) are the non-diagonal terms of the normalised weighted covariance matrix, (C4).

Appendix D. Wavenumber model

The model introduced here $k_\parallel \sim k_\perp^\alpha$ is generalised from the critical balance model of Alfvénic turbulence (Goldreich & Sridhar 1995). In this Letter it is used to model the compressive wave propagation angle $\theta_{\hat{\boldsymbol{b}},\hat{\boldsymbol{k}}}$. To ensure the isotropic wavenumber ($k_{\rm iso} = k$ when $k_\perp = k_\parallel$) is defined correctly

$$\frac{k_\parallel}{k_{\rm iso}/\sqrt{2}} = \left(\frac{k_\perp}{k_{\rm iso}/\sqrt{2}}\right)^\alpha, \tag{D1}$$

which leads to

$$k = \frac{k_{\rm iso}}{\sqrt{2}} \cos(\theta_{\hat{\boldsymbol{b}},\hat{\boldsymbol{k}}})^{1/(\alpha-1)} \sin(\theta_{\hat{\boldsymbol{b}},\hat{\boldsymbol{k}}})^{\alpha/(1-\alpha)}, \tag{D2}$$

which appears as (4.1). Here, k depends on $\theta_{\hat{\boldsymbol{b}},\hat{\boldsymbol{k}}}$ parametrised by $\alpha \in [0, 1),\ k_{\rm iso}$. Equation (D2) can be inverted on $\theta_{\hat{\boldsymbol{b}},\hat{\boldsymbol{k}}} \in [0, 90^\circ)$ for k.

The wavenumber model is also used in the derivation of (4.4) of the Letter. Just above (4.4) the relation

$$k_\parallel^{\rm trans} \lambda_{\rm mfp}^{\rm eff} = v_{\rm th}^{\rm p}/c_{\rm s}, \tag{D3}$$

https://doi.org/10.1017/S0022377822000836 Published online by Cambridge University Press

is argued to define $k_{\parallel}^{\rm trans}$, which can be compared with measurements with the full wavenumber $k^{\rm trans}$. Using the model, (D2), to write

$$\frac{v_{\rm th}^{\rm p}}{c_{\rm s}\,\lambda_{\rm mfp}^{\rm eff}} = k^{\rm trans}\cos(\theta_{\hat{\boldsymbol{b}},\hat{\boldsymbol{k}}}^{\rm trans}) = \frac{k_{\rm iso}}{\sqrt{2}}\tan(\theta_{\hat{\boldsymbol{b}},\hat{\boldsymbol{k}}}^{\rm trans})^{\alpha/(1-\alpha)}, \tag{D4}$$

solving for $\theta_{\hat{\boldsymbol{b}},\hat{\boldsymbol{k}}}^{\rm trans}$

$$\theta_{\hat{\boldsymbol{b}},\hat{\boldsymbol{k}}}^{\rm trans} = \arctan\left\{\left[\frac{\sqrt{2}v_{\rm th}^{\rm p}}{c_{\rm s}\,k_{\rm iso}\,\lambda_{\rm mfp}^{\rm eff}}\right]^{(1-\alpha)/\alpha}\right\}, \tag{D5}$$

then $k^{\rm trans}$ can be written

$$k^{\rm trans} = \frac{k_{\rm iso}}{\sqrt{2}}\cos(\theta_{\hat{\boldsymbol{b}},\hat{\boldsymbol{k}}}^{\rm trans})^{1/\alpha-1}\sin(\theta_{\hat{\boldsymbol{b}},\hat{\boldsymbol{k}}}^{\rm trans})^{\alpha/1-\alpha}. \tag{D6}$$

Using trigonometric identities the transition wavenumber is,

$$k^{\rm trans} = \frac{v_{\rm th}^{\rm p}}{c_{\rm s}\,\lambda_{\rm mfp}^{\rm eff}}\sqrt{1+\left[\frac{2(v_{\rm th}^{\rm p})^2}{c_{\rm s}^2\,k_{\rm iso}^2\,(\lambda_{\rm mfp}^{\rm eff})^2}\right]^{(1-\alpha)/\alpha}}. \tag{D7}$$

This appears as (4.4) of the letter.

REFERENCES

Bale, S.D., Kasper, J.C., Howes, G.G., Quataert, E., Salem, C. & Sundkvist, D. 2009 Magnetic fluctuation power near proton temperature anisotropy instability thresholds in the solar wind. *Phys. Rev. Lett.* **103** (21), 211101.

Barnes, A. 1966 Collisionless damping of hydromagnetic waves. *Phys. Fluids* **9** (8), 1483–1495.

Bhatnagar, P.L., Gross, E.P. & Krook, M. 1954 A model for collision processes in gases. I. Small amplitude processes in charged and neutral one-component systems. *Phys. Rev.* **94** (3), 511–525.

Bruno, R. & Carbone, V. 2013 The solar wind as a turbulence laboratory. *Living Rev. Sol. Phys.* **10** (1), 2.

Chandran, B.D.G., Dennis, T.J., Quataert, E. & Bale, S.D. 2011 Incorporating kinetic physics into a two-fluid solar-wind model with temperature anisotropy and low-frequency Alfven-wave turbulence. *Astrophys. J.* **743** (2), 197.

Chen, C.H.K. 2016 Recent progress in astrophysical plasma turbulence from solar wind observations. *J. Plasma Phys.* **82** (6), 535820602.

Chen, C.H.K., Mallet, A., Schekochihin, A.A., Horbury, T.S., Wicks, R.T. & Bale, S.D. 2012 Three-dimensional structure of solar wind turbulence. *Astrophys. J.* **758** (2), 120.

Chen, C.H.K., Matteini, L., Schekochihin, A.A., Stevens, M.L., Salem, C.S., Maruca, B.A., Kunz, M.W. & Bale, S.D. 2016 Multi-species measurements of the firehose and mirror instability thresholds in the solar wind. *Astrophys. J. Lett.* **825** (2), L26.

Chew, G.F., Goldberger, M.L. & Low, F.E. 1956 The Boltzmann equation and the one-fluid hydromagnetic equations in the absence of particle collisions. *Proc. R. Soc. Lond.* A **236** (1204), 112–118.

Coburn, J.T., Smith, C.W., Vasquez, B.J., Stawarz, J.E. & Forman, M.A. 2012 The turbulent cascade and proton heating in the solar wind during solar minimum. *Astrophys. J.* **754** (2), 93.

Coleman, P.J. Jr., 1968 Turbulence, viscosity, and dissipation in the solar-wind plasma. *Astrophys. J.* **153**, 371.

Coroniti, F.V. & Eviatar, A. 1977 Magnetic field reconnection in a collisionless plasma. *Astrophys. J. Suppl.* **33**, 189–210.

https://doi.org/10.1017/S0022377822000836 Published online by Cambridge University Press

FRIED, B.D. & CONTE, S.D. 2015 *The Plasma Dispersion Function: The Hilbert Transform of the Gaussian*. Academic.

GARY, S.P., YIN, L. & WINSKE, D. 2000 Electromagnetic proton cyclotron anisotropy instability: wave-particle scattering rate. *Geophys. Res. Lett*. **27** (16), 2457–2459.

GOLDREICH, P. & SRIDHAR, S. 1995 Toward a theory of interstellar turbulence. II. Strong Alfvenic turbulence. *Astrophys. J*. **438**, 763.

GOLDREICH, P. & SRIDHAR, S. 1997 Magnetohydrodynamic turbulence revisited. *Astrophys. J*. **485** (2), 680–688.

GRAHAM, D.B., KHOTYAINTSEV, Y.V., ANDRÉ, M., VAIVADS, A., DIVIN, A., DRAKE, J.F., NORGREN, C., CONTEL, O.L., LINDQVIST, P.-A., RAGER, A.C., *et al.* 2022 Direct observations of anomalous resistivity and diffusion in collisionless plasma. *Nat. Commun*. **13** (1), 2954.

GRIFFEL, D.H. & DAVIS, L. 1969 The anisotrophy of the solar wind. *Planet. Space Sci*. **17** (5), 1009–1020.

GROŠELJ, D., CHEN, C.H., MALLET, A., SAMTANEY, R., SCHNEIDER, K. & JENKO, F. 2019 Kinetic turbulence in astrophysical plasmas: waves and/or structures? *Phys. Rev.* X **9** (3), 031037.

GROSS, E.P. & KROOK, M. 1956 Model for collision processes in gases: small-amplitude oscillations of charged two-component systems. *Phys. Rev*. **102** (3), 593–604.

HAMASAKI, S. & KRALL, N.A. 1973 Relaxation of anisotropic collisionless plasma. *Phys. Fluids* **16** (1), 145–149.

HELANDER, P., STRUMIK, M. & SCHEKOCHIHIN, A.A. 2016 Constraints on dynamo action in plasmas. *J. Plasma Phys*. **82** (6), 905820601.

HELLINGER, P., TRÁVNÍČEK, P., KASPER, J.C. & LAZARUS, A.J. 2006 Solar wind proton temperature anisotropy: linear theory and WIND/SWE observations. *Geophys. Res. Lett*. **33** (9), L09101.

HELLINGER, P., TRÁVNÍČEK, P.M., ŠTVERÁK, V., MATTEINI, L. & VELLI, M. 2013 Proton thermal energetics in the solar wind: helios reloaded. *J. Geophys. Res*. **118** (4), 1351–1365.

HOWES, G.G., BALE, S.D., KLEIN, K.G., CHEN, C.H.K., SALEM, C.S. & TENBARGE, J.M. 2012 The slow-mode nature of compressible wave power in solar wind turbulence. *Astrophys. J. Lett*. **753** (1), L19.

HOWES, G.G., COWLEY, S.C., DORLAND, W., HAMMETT, G.W., QUATAERT, E. & SCHEKOCHIHIN, A.A. 2006 Astrophysical gyrokinetics: basic equations and linear theory. *Astrophys. J*. **651** (1), 590–614.

HUBA J. D. 1983 NRL (Naval Research Laboratory) plasma formulary, revised. *Tech. Rep.* Naval Research Lab, Washington DC.

HUNANA, P., TENERANI, A., ZANK, G.P., KHOMENKO, E., GOLDSTEIN, M.L., WEBB, G.M., CALLY, P.S., COLLADOS, M., VELLI, M. & ADHIKARI, L. 2019 An introductory guide to fluid models with anisotropic temperatures. Part 1. CGL description and collisionless fluid hierarchy. *J. Plasma Phys*. **85** (6), 205850602.

KASPER, J.C., LAZARUS, A.J. & GARY, S.P. 2002 Wind/SWE observations of firehose constraint on solar wind proton temperature anisotropy. *Geophys. Res. Lett*. **29** (17), 1839.

KELLOGG, P.J. 2000 Fluctuations and ion isotropy in the solar wind. *Astrophys. J*. **528** (1), 480–485.

KELLOGG, P.J. & HORBURY, T.S. 2005 Rapid density fluctuations in the solar wind. *Ann. Geophys*. **23** (12), 3765.

KENDALL, M.G. & STUART, A. 1977 *The Advanced Theory of Statistics. Vol. 1: Distribution Theory*. Macmillan.

KIYANI, K.H., OSMAN, K.T. & CHAPMAN, S.C. 2015 Dissipation and heating in solar wind turbulence: from the macro to the micro and back again. *Phil. Trans. R. Soc. Lond.* A **373** (2041), 20140155.

KLEIN, K.G., HOWES, G.G., TENBARGE, J.M., BALE, S.D., CHEN, C.H.K. & SALEM, C.S. 2012 Using synthetic spacecraft data to interpret compressible fluctuations in solar wind turbulence. *Astrophys. J*. **755** (2), 159.

KULSRUD, R.M., SAGDEEV, R.N. & ROSENBLUTH, M.N. 1980 *MHD Description of Plasma: Handbook of Plasma Physics*. North–Holland.

KUNZ, M.W., SCHEKOCHIHIN, A.A. & STONE, J.M. 2014 Firehose and mirror instabilities in a collisionless shearing plasma. *Phys. Rev. Lett*. **112** (20), 205003.

KUNZ, M.W., SQUIRE, J., SCHEKOCHIHIN, A.A. & QUATAERT, E. 2020 Self-sustaining sound in collisionless, high-β plasma. *J. Plasma Phys*. **86** (6), 905860603.

KUNZ, M.W., STONE, J.M. & QUATAERT, E. 2016 Magnetorotational turbulence and dynamo in a collisionless plasma. *Phys. Rev. Lett*. **117** (23), 235101.

LEAMON, R.J., SMITH, C.W., NESS, N.F., MATTHAEUS, W.H. & WONG, H.K. 1998 Observational constraints on the dynamics of the interplanetary magnetic field dissipation range. *J. Geophys. Res*. **103** (A3), 4775–4787.

LEPPING, R., ACŨNA, M., BURLAGA, L., FARRELL, W., SLAVIN, J., SCHATTEN, K., MARIANI, F., NESS, N., NEUBAUER, F., WHANG, Y., *et al.* 1995 The wind magnetic field investigation. *Space Sci. Rev*. **71** (1-4), 207–229.

LIN, R.P., ANDERSON, K.A., ASHFORD, S., CARLSON, C., CURTIS, D., ERGUN, R., LARSON, D., MCFADDEN, J., MCCARTHY, M., PARKS, G.K., *et al.* 1995 A three-dimensional plasma and energetic particle investigation for the wind spacecraft. *Space Sci. Rev*. **71** (1–4), 125–153.

LITHWICK, Y. & GOLDREICH, P. 2001 Compressible magnetohydrodynamic turbulence in interstellar plasmas. *Astrophys. J*. **562** (1), 279–296.

MACBRIDE, B.T., SMITH, C.W. & FORMAN, M.A. 2008 The turbulent cascade at 1 AU: energy transfer and the third-order scaling for MHD. *Astrophys. J*. **679** (2), 1644–1660.

MARSCH, E. 2006 Kinetic physics of the solar corona and solar wind. *Living Rev. Sol. Phys*. **3** (1), 1.

MARSCH, E., MUEHLHAEUSER, K.H., ROSENBAUER, H. & SCHWENN, R. 1983 On the equation of state of solar wind ions derived from helios measurements. *J. Geophys Res*. **88** (A4), 2982–2992.

MARSCH, E. & TU, C.Y. 1990 Spectral and spatial evolution of compressible turbulence in the inner solar wind. *J. Geophys. Res*. **95** (A8), 11945–11956.

MATTEINI, L., HELLINGER, P., LANDI, S., TRÁVNÍČEK, P.M. & VELLI, M. 2012 Ion kinetics in the solar wind: coupling global expansion to local microphysics. *Space Sci. Rev*. **172** (1–4), 373–396.

MATTHAEUS, W.H., DASSO, S., WEYGAND, J.M., KIVELSON, M.G. & OSMAN, K.T. 2010 Eulerian decorrelation of fluctuations in the interplanetary magnetic field. *Astrophys. J. Lett*. **721** (1), L10–L13.

MATTHAEUS, W.H. & GOLDSTEIN, M.L. 1982 Measurement of the rugged invariants of magnetohydrodynamic turbulence in the solar wind. *J. Geophys. Res*. **87** (A8), 6011–6028.

MATTHAEUS, W.H., ZANK, G.P., SMITH, C.W. & OUGHTON, S. 1999 Turbulence, spatial transport, and heating of the solar wind. *Phys. Rev. Lett*. **82** (17), 3444–3447.

MEYRAND, R., KANEKAR, A., DORLAND, W. & SCHEKOCHIHIN, A.A. 2019 Fluidization of collisionless plasma turbulence. *Proc. Natl Acad. Sci. USA* **116** (4), 1185–1194.

MONTGOMERY, D., BROWN, M.R. & MATTHAEUS, W.H. 1987 Density fluctuation spectra in magnetohydrodynamic turbulence. *J. Geophys. Res*. **92** (A1), 282–284.

NICOLAOU, G., LIVADIOTIS, G., WICKS, R.T., VERSCHAREN, D. & MARUCA, B.A. 2020 Polytropic behavior of solar wind protons observed by Parker solar probe. *Astrophys. J*. **901** (1), 26.

NISHIDA, A. 1969 Thermal state and effective collision frequency in the solar wind plasma. *J. Geophys. Res*. **74** (21), 5155.

NORRIS, N. 1940 The standard errors of the geometric and harmonic means and their application to index numbers. *Ann. Stat*. **11** (4), 445–448.

PARKER, E.N. 1958 Dynamics of the interplanetary gas and magnetic fields. *Astrophys. J*. **128**, 664.

PEZZI, O., PERRONE, D., SERVIDIO, S., VALENTINI, F., SORRISO-VALVO, L. & VELTRI, P. 2019 Proton–proton collisions in the turbulent solar wind: hybrid Boltzmann–Maxwell simulations. *Astrophys. J*. **887** (2), 208.

PEZZI, O., VALENTINI, F. & VELTRI, P. 2016 Collisional relaxation of fine velocity structures in plasmas. *Phys. Rev. Lett*. **116** (14), 145001.

QUATAERT, E. 2003 Radiatively inefficient accretion flow models of Sgr A*. *Astron. Nachr*. **324** (1), 435–443.

RINCON, F., CALIFANO, F., SCHEKOCHIHIN, A.A. & VALENTINI, F. 2016 Turbulent dynamo in a collisionless plasma. *Proc. Natl Acad. Sci. USA* **113** (15), 3950–3953.

SCHEKOCHIHIN, A.A. & COWLEY, S.C. 2006 Turbulence, magnetic fields, and plasma physics in clusters of galaxies. *Phys. Plasmas* **13** (5), 056501.

SCHEKOCHIHIN, A.A., COWLEY, S.C., DORLAND, W., HAMMETT, G.W., HOWES, G.G., QUATAERT, E. & TATSUNO, T. 2009 Astrophysical gyrokinetics: kinetic and fluid turbulent cascades in magnetized weakly collisional plasmas. *Astrophys. J. Suppl*. **182** (1), 310–377.

SCHEKOCHIHIN, A.A., COWLEY, S.C., KULSRUD, R.M., HAMMETT, G.W. & SHARMA, P. 2005 Plasma instabilities and magnetic field growth in clusters of galaxies. *Astrophys. J.* **629** (1), 139–142.

SCHEKOCHIHIN, A.A., PARKER, J.T., HIGHCOCK, E.G., DELLAR, P.J., DORLAND, W. & HAMMETT, G.W. 2016 Phase mixing versus nonlinear advection in drift-kinetic plasma turbulence. *J. Plasma Phys.* **82** (2), 905820212.

SHARMA, P., HAMMETT, G.W. & QUATAERT, E. 2003 Transition from collisionless to collisional magnetorotational instability. *Astrophys. J.* **596** (2), 1121–1130.

SNYDER, P.B., HAMMETT, G.W. & DORLAND, W. 1997 Landau fluid models of collisionless magnetohydrodynamics. *Phys. Plasmas* **4** (11), 3974–3985.

SPITZER, L. 1962 *Physics of Fully Ionized Gases*. Courier Corporation.

SQUIRE, J., KUNZ, M.W., QUATAERT, E. & SCHEKOCHIHIN, A.A. 2017 Kinetic simulations of the interruption of large-amplitude shear-Alfvén waves in a high-β plasma. *Phys. Rev. Lett.* **119** (15), 155101.

SQUIRE, J., QUATAERT, E. & KUNZ, M.W. 2017 Pressure-anisotropy-induced nonlinearities in the kinetic magnetorotational instability. *J. Plasma Phys.* **83** (6), 905830613.

STAWARZ, J.E., SMITH, C.W., VASQUEZ, B.J., FORMAN, M.A. & MACBRIDE, B.T. 2009 The turbulent cascade and proton heating in the solar wind at 1 AU. *Astrophys. J.* **697** (2), 1119–1127.

TAYLOR, G.I. 1938 The spectrum of turbulence. *Proc. R. Soc. Lond.* A **164** (919), 476–490.

TOTTEN, T.L., FREEMAN, J.W. & ARYA, S. 1995 An empirical determination of the polytropic index for the free-streaming solar wind using Helios 1 data. *J. Geophys. Res.* **100** (A1), 13–18.

TU, C.-Y. & MARSCH, E. 1995 Mhd structures, waves and turbulence in the solar wind: observations and theories. *Space Sci. Rev.* **73** (1–2), 1–210.

TU, C.Y. & MARSCH, E. 2002 Anisotropy regulation and plateau formation through pitch angle diffusion of solar wind protons in resonance with cyclotron waves. *J. Geophys Res.* **107** (A9), 1249.

VASQUEZ, B.J., SMITH, C.W., HAMILTON, K., MACBRIDE, B.T. & LEAMON, R.J. 2007 Evaluation of the turbulent energy cascade rates from the upper inertial range in the solar wind at 1 AU. *J. Geophys. Res.* **112** (A7), A07101.

VERMA, M.K., ROBERTS, D.A. & GOLDSTEIN, M.L. 1995 Turbulent heating and temperature evolution in the solar wind plasma. *J. Geophys. Res.* **100** (A10), 19839–19850.

VERSCHAREN, D., CHANDRAN, B.D.G., KLEIN, K.G. & QUATAERT, E. 2016 Collisionless isotropization of the solar-wind protons by compressive fluctuations and plasma instabilities. *Astrophys. J.* **831** (2), 128.

VERSCHAREN, D., CHEN, C.H.K. & WICKS, R.T. 2017 On kinetic slow modes, fluid slow modes, and pressure-balanced structures in the solar wind. *Astrophys. J.* **840** (2), 106.

VERSCHAREN, D., KLEIN, K.G. & MARUCA, B.A. 2019 The multi-scale nature of the solar wind. *Living Rev. Sol. Phys.* **16** (1), 5.

YAO, S., HE, J.S., MARSCH, E., TU, C.Y., PEDERSEN, A., RÈME, H. & TROTIGNON, J.G. 2011 Multi-scale anti-correlation between electron density and magnetic field strength in the solar wind. *Astrophys. J.* **728** (2), 146.

YAO, S., HE, J.S., TU, C.Y., WANG, L.H. & MARSCH, E. 2013*a* Small-scale pressure-balanced structures driven by mirror-mode waves in the solar wind. *Astrophys. J.* **776** (2), 94.

YAO, S., HE, J.S., TU, C.Y., WANG, L.H. & MARSCH, E. 2013*b* Small-scale pressure-balanced structures driven by oblique slow mode waves measured in the solar wind. *Astrophys. J.* **774** (1), 59.

YOON, P.H. 2017 Kinetic instabilities in the solar wind driven by temperature anisotropies. *Rev. Mod. Plasma Phys.* **1** (1), 4.

ZANK, G.P., MATTHAEUS, W.H. & SMITH, C.W. 1996 Evolution of turbulent magnetic fluctuation power with heliospheric distance. *J. Geophys. Res.* **101** (A8), 17093–17108.

ZHURAVLEVA, I., CHURAZOV, E., SCHEKOCHIHIN, A.A., ALLEN, S.W., VIKHLININ, A. & WERNER, N. 2019 Suppressed effective viscosity in the bulk intergalactic plasma. *Nat. Astron.* **3**, 832–837.